Existence of an ^{16}O-Rich Gaseous Reservoir in the Solar Nebula

Alexander N. Krot,[1]* Kevin D. McKeegan,[2] Laurie A. Leshin,[3] Glenn J. MacPherson,[4] Edward R. D. Scott[1]

Carbonaceous chondrite condensate olivine grains from two distinct petrographic settings, calcium-aluminum–rich inclusion (CAI) accretionary rims and amoeboid olivine aggregates (AOAs), are oxygen-16 (^{16}O) enriched at the level previously observed inside CAIs. This requires that the gas in the nebular region where these grains condensed was ^{16}O-rich. This contrasts with an ^{16}O-poor gas present during the formation of chondrules, suggesting that CAIs and AOAs formed in a spatially restricted region of the solar nebula containing ^{16}O-rich gas. The ^{16}O-rich gas composition may have resulted either from mass-independent isotopic chemistry or from evaporation of regions with enhanced dust/gas ratios, possibly in an X-wind environment near the young Sun.

Chondrite meteorites (chondrites) preserve records of physical and chemical processes that occurred during the earliest stages of solar system evolution. Chondrites are made up of three major components: refractory CAIs, less refractory Fe-Mg-silicate spherules called chondrules, and a fine-grained matrix that is richer in volatile elements. CAIs and chondrules formed by high-temperature processes including condensation, evaporation, and, for chondrules and many CAIs, subsequent melting of the early condensates during multiple, brief heating episodes (*1–3*). Mineralogical and bulk chemical differences between CAIs and chondrules suggest that CAIs formed from materials that were processed at higher nebular temperatures, whereas the matrix escaped any substantial high-temperature processing (*4*). How such mineralogically diverse objects, which experienced distinct thermal histories, came to coexist in chondrites presents a major challenge for models of the formation and early evolution of planetary materials in the solar nebula (*5, 6*).

Isotopic abundances can provide important constraints on the origin of the chondritic components. For example, CAIs and chondrules formed with different initial contents of the short-lived radionuclide ^{26}Al (*7–10*), indicating either that CAIs formed at least 2 million years (Ma) earlier than chondrules (*8–10*) or, alternatively, that the two groups

of objects formed contemporaneously in isotopically distinct and spatially separated nebular reservoirs (*5*). Oxygen-isotopic compositions hint that CAIs and chondrules formed in different places (*11*). Most CAIs from several classes of chondrites have similar ^{16}O-rich isotopic compositions [$\delta^{17,18}$O ∼ −50 per mil (‰)] (*11–15*). Chondrules, in contrast, have relatively ^{16}O-poor isotopic compositions (−10‰ < $\delta^{17,18}$O < 5‰) that vary between ordinary, carbonaceous, and enstatite chondrite classes (*16, 17*). The consistency of CAI oxygen-isotopic compositions relative to that of chondrules has been used to argue that CAIs formed in a single,

restricted nebular site and were subsequently distributed and mixed with matrix and chondrules in the chondrite accretion regions (*11, 18*).

Understanding the relationship between the two isotopic reservoirs is crucial to understanding the evolution of early solar system materials. Two types of ferromagnesian material associated with CAIs may be links between CAIs and chondrules and, hence, their respective isotopic reservoirs: (i) olivine-rich accretionary rims (*19*) outside the Wark-Lovering rims on CAIs (*20*) and (ii) AOAs that occur as separate objects in chondrites and are associated with refractory minerals (*21, 22*). To better assess the possible genetic and spatial relationships between CAIs, accretionary and Wark-Lovering rims, AOAs, and chondrules, we used an ion microprobe to analyze in situ the oxygen-isotopic compositions of minerals in two CAIs and their surrounding rims from Efremovka and Vigarano and in an Efremovka AOA (*23*).

Efremovka E104 is an irregularly shaped, type A CAI composed of melilite, Al-diopside, spinel, and perovskite (Fig. 1). The CAI is surrounded by a thin (∼25 μm) multilayered Wark-Lovering rim sequence of spinel, anorthite, and Al-diopside. Outside of the Wark-Lovering rim is an accretionary rim up to 500 μm thick that fills in topographic depressions on the surface of the CAI, similar to accretionary rims around Allende CAIs (*22*). It is a porous aggregate of forsterite crystals, FeNi-metal, and small refractory regions consisting of Al-diopside, anorthite, and minor spinel (Fig. 2A). The olivine crys-
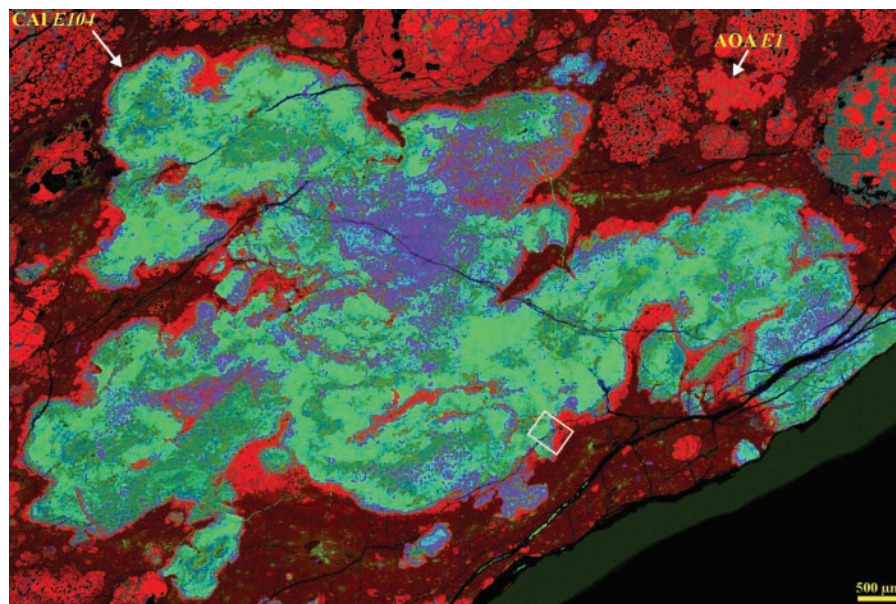
[1]Hawaii Institute of Geophysics and Planetology, School of Ocean and Earth Science and Technology, University of Hawaii, Honolulu, HI 96822, USA. [2]Department of Earth and Space Sciences, University of California, Los Angeles, Los Angeles, CA 90095–1567, USA. [3]Department of Geological Sciences, Arizona State University, Tempe, AZ 85287–1404, USA. [4]Department of Mineral Sciences, U.S. National Museum of Natural History, Smithsonian Institution, Washington, DC 20560–0119, USA.

*To whom correspondence should be addressed. E-mail: sasha@higp.hawaii.edu

Fig. 1. Combined x-ray map composed of Mg Kα (red), Ca Kα (green), and Al Kα (blue) of a polished section of the Efremovka meteorite containing Ca, Al-rich inclusion E104, and amoeboid olivine aggregate E1. The CAI consists of spinel (purple), Al-diopside (dark green), anorthite (light blue), and melilite (light green). It is surrounded by a multilayered Wark-Lovering rim and a thick forsterite-rich rim (red). The outlined region is shown in detail in Fig. 2A.

tals contain abundant tiny inclusions of Al-diopside (Fig. 2B). Vigarano 1623-2 is an elliptical-shaped type A CAI containing mostly melilite, with abundant spinel and hibonite, and accessory perovskite and FeNi beads. Secondary minerals include calcite, which occurs along fractures, and rare anorthite and nepheline. The inclusion is surrounded by Wark-Lovering rim layers consisting of spinel, Al-diopside, and forsterite. Outside of the Wark-Lovering rim sequence is a discontinuous accretionary rim consisting mostly of fine-grained forsterite. Efremovka E1 is an irregularly shaped AOA composed of forsterite crystals and dispersed regions consisting of Al-diopside, anorthite, and minor spinel.

The oxygen isotope data (Table 1; Fig. 3A) for Efremovka E104 exhibit a bimodal distribution: Spinel and pyroxene in both the CAI and its Wark-Lovering rim, as well as coarse-grained forsterite in the accretionary rim, have similar ^{16}O-rich compositions, but melilite is ^{16}O-poor and plots near terrestrial fractionation line. Small variations in oxygen-isotopic compositions of pyroxenes result from overlap of ion probe spots onto neighboring melilite and anorthite. Similar variations in the composition of fine-grained forsterite in the accretionary rims probably reflect beam overlap onto isotopically heavy, secondary ferrous olivine rims along forsterite grain boundaries (24). The data for Vigarano 1623-2 (Table 1; Fig. 3B) show a similar bimodal distribution: Spinel and hibonite are ^{16}O-rich ($\delta^{17,18}O \sim -40$ to -50‰), and melilite plots near the ^{16}O-depleted end of the Allende CAI line. Spinel in the Wark-Lovering rim and forsterite in the overlying accretionary rim are isotopically indistinguishable from interior spinel grains. The pyroxene layer shows a relatively broad range in oxygen-isotopic composition ($\delta^{17,18}O \sim -20$ to -40‰). Forsterite in the AOA E1 (Table 1; Fig. 3A) is enriched in ^{16}O to a level similar to that found in the forsterite-rich accretionary rims on E104 and 1629-2. Hiyagon and Hashimoto (25) suggested that ^{16}O-enriched olivine is relatively common in carbonaceous chondrites on the basis of measurements of eight forsterite-rich olivine inclusions in the Murchison (CM2) and Yamato-86009 (CV3) meteorites. Our results on the AOA E1, which is petrographically similar to their olivine inclusions, support this conclusion.

The accretionary rims consist of minerals such as forsterite, Al-diopside, and FeNi metal that are less refractory than their underlying melilite-rich CAIs. The porous aggregation textures of coarse forsterite grains in the accretionary rims and the similar estimated condensation temperatures [at total pressure (P_{tot}) $\sim 10^{-5}$ bar] of diopside (1323 K), forsterite (1318 K), and FeNi-metal (1290 K) (26) are consistent with the interpretation that forsterite-rich accretionary rim layers are aggregates of condensate particles (19). Similar
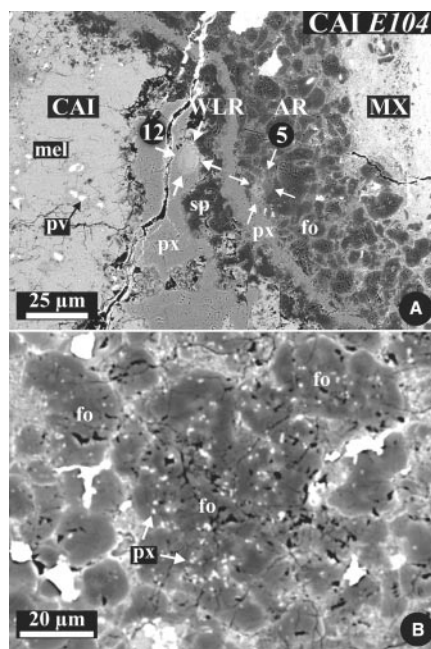

Fig. 2. (**A** and **B**) Backscattered electron images of a region of the CAI E104 outlined in Fig. 1. Craters produced by ion microprobe are indicated by arrows; numbers correspond to number of analysis listed in Table 1. AR, accretionary rim; WLR, Wark-Lovering rims; MX, matrix; fo, forsterite; mel, melilite; pv, perovskite; px, Al-diopside; sp, spinel. Backscattered electron images of AOA E1 are available on *Science* Online (38).

textures and mineralogy in AOAs suggest a close genetic association between these objects and the forsterite-rich accretionary rim layers. The ^{16}O enrichment in AOA E1 supports this association.

If the interpretation is correct that the forsterite in the accretionary rims and AOAs formed by condensation, then the nebular gas from which they condensed must have been ^{16}O-rich. Likewise, the ^{16}O-rich compositions of minerals in the Wark-Lovering rims, which have been interpreted as the products of gas-solid exchange between the CAI and the nebula (27, 28), indicate the presence of ^{16}O-rich gas. The existence of an ^{16}O-rich gas in the nebula has been postulated (29) on the basis of the general ^{16}O-rich nature of CAIs (16). However, most workers interpret the ^{16}O-mixing trends observed in meteorites as resulting from interactions between an ^{16}O-poor gaseous reservoir and an ^{16}O-rich solid reservoir [e.g., (16, 30)]. Our results require the contrary, i.e., that a separate ^{16}O-rich gaseous reservoir existed in the region where CAIs, their rims, and olivine-rich inclusions formed (31). It follows that this region was different from the ^{16}O-poor reservoir that is recorded by the isotopic composition of chondrules (16, 17). One possibility is that the two regions were physically separated, which is consistent with the rarity of petrologic evidence for CAIs being present during the
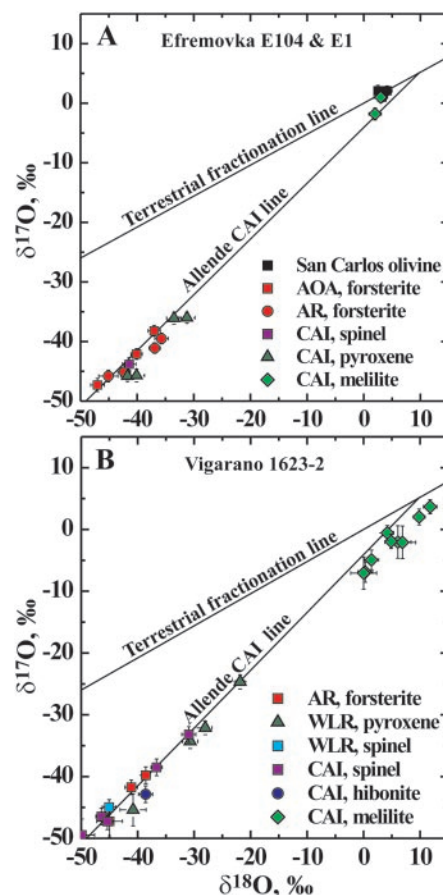

Fig. 3. Oxygen-isotopic compositions of minerals in the Efremovka CAI E104, AOA E1, and San Carlos (terrestrial) olivine (**A**) and Vigarano CAI 1623-2 (**B**).

melting and reprocessing of chondrules (32).

Two mechanisms for generating ^{16}O-rich gas in the solar nebula have been proposed. Thiemens (33) showed that a purely chemical, gaseous processes can lead to non–mass-dependent isotopic fractionation. These mass-independent processes have been found to occur in the atmospheres of Earth and Mars at low temperatures, and this signature has been transferred to the rock record on both planets (33). In a high-temperature solar nebular setting, however, a mechanism for generating non–mass-dependent isotopic effects and incorporating them into condensing solids has not yet been established. Hiyagon and Hashimoto (25) pointed out additional problems with the Thiemens model (33) and interpreted their ^{16}O-rich forsterite inclusions to be the result of unspecified non–mass-dependent chemical processes in the nebula.

Alternatively, an ^{16}O-rich gaseous reservoir could have been produced by evaporating ^{16}O-rich presolar solid materials in nebular regions of enhanced, ~ 20 to 50 times solar, dust:gas ratio (6, 29). The term "dust" is defined here as a solid phase containing all elements in cosmic proportion, with the exception of hydrogen and the noble gases. This degree of dust enrichment

Table 1. Oxygen-isotopic compositions of minerals in the Efremovka and Vigarano CAIs, AOA, Wark-Lovering and forsterite-rich accretionary rims. an, anorthite; fo, forsterite; hib, hibonite; mel, melilite; px, pyroxene; pv, perovskite; sp, spinel; fgr, fine grained; cgr, coarse grained; AR, accretionary rim; WLR, Wark-Lovering rim.

Mineral	Spot	Object	$\delta^{18}O$ (‰)	1σ (‰)	$\delta^{17}O$ (‰)	1σ (‰)
			Efremovka E1			
fo+an+px	1	AOA	−37.0	1.1	−38.2	0.9
fo+an+px	2	AOA	−40.1	1.0	−42.1	0.9
fo, cgr	3	AOA	−47.0	1.2	−47.3	1.1
			Efremovka E104			
fo, fgr	4	AR	−35.7	1.2	−39.5	0.9
fo, frg	5	AR	−36.9	1.0	−41.1	0.9
fo, cgr	6	AR	−42.3	1.1	−45.1	1.2
fo, cgr	7	AR	−45.1	1.7	−45.8	1.0
px	8	WLR	−40.1	1.4	−45.7	1.1
sp	9	CAI	−41.4	1.2	−43.8	1.1
px+mel	10	CAI	−31.2	1.4	−36.0	0.9
px+an	11	CAI	−33.5	1.3	−36.1	1.0
px	12	CAI	−41.7	1.2	−45.8	0.9
mel	13	CAI	6.3	1.1	−1.8	1.0
mel	14	CAI	7.9	1.2	1.0	0.9
			Vigarano 1623-2			
fo	1	AR	−38.6	0.8	−39.8	1.4
fo	2	AR	−41.1	1.1	−41.7	1.2
fo	3	AR	−45.0	2.3	−47.2	2.6
px	4	WLR	−21.9	0.8	−24.7	1.1
px	5	WLR	−28.0	1.2	−32.1	1.1
px	6	WLR	−30.7	1.4	−34.3	1.2
px	7	WLR	−40.8	2.3	−45.4	2.6
sp	8	WLR	−45.1	1.2	−45.0	1.2
sp+mel+pv+hib	9	CAI	−31.0	1.2	−33.2	1.3
sp+mel+pv	10	CAI	−36.7	1.0	−38.5	1.4
hib+mel	11	CAI	−38.6	1.3	−42.9	1.4
sp+pv+mel	12	CAI	−45.4	1.0	−47.3	1.3
sp	13	CAI	−46.4	1.0	−46.5	1.4
sp	14	CAI	−49.9	2.3	−49.5	2.6
sp	15	CAI	−52.4	2.3	−52.4	2.7
mel, interior	16	CAI	0.0	2.3	−7.1	2.6
mel, interior	17	CAI	0.3	1.3	−6.9	1.6
mel, interior	18	CAI	1.4	1.3	−4.9	1.6
mel, interior	19	CAI	4.2	1.1	−0.6	1.2
mel, interior	20	CAI	9.8	1.0	2.0	1.3
mel, near WLR	21	CAI	4.9	0.7	−1.9	1.2
mel, near WLR	22	CAI	6.1	2.3	−2.0	2.6
mel, near WLR	23	CAI	6.9	2.4	−2.1	2.6
mel, near WLR	24	CAI	11.8	1.2	3.7	1.2

does not change the predicted nebular condensation sequence of minerals or our conclusion that accretionary rims are nebular condensates (*34, 35*). Two different astrophysical settings have been proposed to explain how ^{16}O-rich dust might have been concentrated relative to ^{16}O-poor nebular gas and then evaporated to generate ^{16}O-rich gas. In a globally hot solar nebula model (*6*), evaporation takes place after coagulation and settling of dust to the hot disk midplane. This model, however, has difficulty producing the transient heating episodes necessary to form some CAIs and chondrules. In the X-wind model (*5*), the dust:gas fractionation occurs beyond the inner edge of the solar accretion disk near the young Sun because of preferential removal of the (^{16}O-poor) ionized nebular gas from this region, followed by thermal processing of the remaining ^{16}O-rich dust (*29, 36*). Chondrules formed slightly farther away from the Sun, in a region of the disk with

an approximately solar dust:gas ratio. Both chondrules and CAIs were subsequently removed from their formation regions by the X-wind. The X-wind astrophysical setting (*5*) near the young Sun is particularly attractive regardless of whether the ^{16}O-rich gas was produced by evaporation or mass-independent isotope fractionation, as it provides a heat source for rapid evaporation, condensation, and transport of thermally processed material to the cold accretionary regions of chondrites.

References and Notes

1. G. J. MacPherson, D. A. Wark, J. T. Armstrong, in *Meteorites and the Early Solar System*, J. F. Kerridge, M. S. Matthews, Eds. (Univ. of Arizona Press, Tucson, AZ, 1988), pp. 746–807.
2. A. E. Rubin, *Earth Sci. Rev.* **50**, 3 (2000).
3. G. J. MacPherson, A. M. Davis, *Geochim. Cosmochim. Acta* **57**, 231 (1993).
4. A. J. Brearley *et al.*, *Geochim. Cosmochim. Acta* **53**, 2081 (1989).
5. F. H. Shu, S. Hsien, T. Lee, *Science* **271**, 1545 (1996).
6. P. Cassen, *Meteorit. Planet. Sci.* **36**, 671 (2001).
7. G. J. MacPherson, A. M. Davis, E. K. Zinner, *Meteoritics* **30**, 365 (1995).
8. S. S. Russell, G. Srinivasan, G. R. Huss, G. J. Wasserburg, G. J. MacPherson, *Science* **273**, 757 (1996).
9. N. T. Kita, H. Nagahara, S. Togashi, Y. Morishita, *Geochim. Cosmochim. Acta* **64**, 3913 (2000).
10. J. A. Wood, in *Chondrules and the Protoplanetary Disk*, R. H. Hewins, R. H. Jones, E. R. D. Scott, Eds. (Cambridge Univ. Press, Cambridge, 1996), pp. 55–69.
11. K. D. McKeegan, L. A. Leshin, S. S. Russell, G. J. MacPherson, *Science* **280**, 414 (1998).
12. $\delta^mO = [(^mO/^{16}O)_{sample}/(^mO/^{16}O)_{SMOW} - 1] \times 1000$ (‰), where $m = 17$ or 18 and SMOW is the standard mean ocean water.
13. R. N. Clayton, L. Grossman, T. K. Mayeda, *Science* **182**, 485 (1973).
14. Y. Guan, K. D. McKeegan, G. J. MacPherson, *Earth Planet. Sci. Lett.* **181**, 271 (2001).
15. T. J. Fagan, K. D. McKeegan, A. N. Krot, K. Keil, *Meteorit. Planet. Sci.* **36**, 223 (2001).
16. R. N. Clayton, *Annu. Rev. Earth Planet. Sci.* **21**, 115 (1993).
17. L. A. Leshin, K. D. McKeegan, G. K. Benedix, *Lunar Planet. Sci* **XXXI**, 1918 (abstract) (2000).
18. A. N. Krot *et al.*, *Meteorit. Planet. Sci.* **34**, A68 (abstract) (1999).
19. G. J. MacPherson, A. Hashimoto, L. Grossman, *Geochim. Cosmochim. Acta* **49**, 2267 (1985). Accretionary rims are stratified porous aggregates of tiny euhedral grains, mostly olivine and calcium-rich pyroxene, that preferentially fill in topographic depressions on the surfaces of the CAIs (outside of the Wark-Lovering rims) on which they occur. The individual crystals within the accretionary rims have been interpreted as nebular condensates. Grain size, mineral chemical, and modal differences distinguish the different rim layers. The innermost layer in many accretionary rims consists of olivine that is consistently coarser grained and more magnesium-rich than in the other layers. In the present report, we analyzed only olivines from this coarser inner layer.
20. Most CAIs are surrounded by thin ($<\sim50$ μm) continuous multilayered rims, first described by D. A. Wark and J. F. Lovering [*Proc. Lunar Sci. Conf.* **8**, 95 (1977)], in which each of the nearly monomineralic layers maintains a constant thickness even around the convoluted peripheries of the most irregularly shaped CAIs.
21. M. Komatsu *et al.*, *Meteorit. Planet. Sci.* **36**, 629 (2001).
22. A. N. Krot, A. A. Ulyanov, A. Meibom, K. Keil, *Meteorit. Planet. Sci.* **36**, 611 (2001).
23. Polished thin sections of Efremovka and Vigarano were studied with optical and scanning electron microscopy (SEM), backscattered electron (BSE) imaging, x-ray elemental mapping, electron probe microanalysis, and ion microprobe. X-ray elemental maps with resolution of 10 μm/pixel were acquired with a Cameca SX-50 electron microprobe at 15-kV accelerating voltage, 100-nA beam current and ~1-μm beam size. BSE images were obtained with a Zeiss DSM-962 scanning electron microscope at 15-kV accelerating voltage and 1- to 2-nA beam current. Wavelength-dispersive element analyses were performed with a Cameca SX-50 electron microprobe at 15-kV accelerating voltage and 10- to 20-nA beam current, with a beam size of ~1 to 2 μm. For each element, counting times on both peak and background were 30 s (10 s for Na). Matrix effects were corrected with PAP (Pouchou and Pichouz) procedures. Oxygen-isotopic ratios were measured in situ with a Cameca ims 1270 ion microprobe operating at a high mass resolution with a beam spot size of ~10 μm; for further details, see (*11*). Results are reported relative to SMOW. Instrumental mass fractionation was corrected with a Burma spinel standard. Under our analytical conditions, possible matrix effects between spinel and the Fe-poor minerals analyzed here are <1 to 2 ‰/atomic mass unit (1σ). The precision and accuracy for a single analysis of each individual spot are in the range 1 to 2‰ for both $\delta^{17}O$ and $\delta^{18}O$. After isotopic analyses, each spot was examined by SEM in BSE mode to verify the location of the sputtered craters and mineralogical compositions of the phases analyzed.

24. H. Imai, H. Yurimoto, *Lunar Planet. Sci.* **XXXII**, 1580 (abstract) (2001).
25. H. Hiyagon, A. Hashimoto, *Science* **283**, 828 (1999).
26. M. I. Petaev, J. A. Wood, *Meteorit. Planet. Sci.* **33**, 1123 (1998).
27. A. M. Davis, G. J. MacPherson, *Meteoritics* **29**, A458 (abstract) (1994).
28. A. Ruzicka, W. V. Boynton, *Meteorit. Planet. Sci.* **30**, 570 (abstract) (1995).
29. E. R. D. Scott, A. N. Krot, *Meteorit. Planet. Sci.* **36**, 1307 (2001).
30. J. A. Wood, *Earth Planet. Sci. Lett.* **56**, 32 (1981).
31. Some minerals within individual CV CAIs, such as melilite and anorthite, have ^{16}O-poor compositions relative to coexisting spinel and pyroxene. If this resulted from gas-solid exchange between the ^{16}O-poor gas and an initially ^{16}O-rich CAI, our results indicate that the exchange probably occurred after the formation of the

Wark-Lovering and accretionary rims. An alternative model (*16, 37*), in which CAIs exchanged with ^{16}O-poor nebular gas during partial remelting and recrystallization, requires a large transient excursion in the isotopic composition of gas in the CAI-forming region in between the time the CAIs formed and the time their Wark-Lovering and accretionary rims formed.
32. The petrologic observations indicating that CAIs were largely absent when Fe-Mg chondrules were melted include (i) absence of relic CAIs inside Fe-Mg chondrules or CAI chondrule compound objects, (ii) preservation of Wark-Lovering rims around most CAIs, and (iii) the slow inferred cooling rates during crystallization of igneous CAIs (1 to 10 K hour^{-1}) compared with those inferred for chondrules (100 to 1000 K hour^{-1}).
33. M. H. Thiemens, *Science* **283**, 341 (1999).
34. J. A. Wood, *Astrophys. J.* **503**, L101 (1998).

35. D. S. Ebel, L. Grossman, *Geochim. Cosmochim. Acta* **64**, 339 (2000).
36. H. Yurimoto, Y. Asada, K. Hirai, *Meteorit. Planet. Sci.* **36**, A230 (abstract) (2001).
37. H. Yurimoto, M. Ito, H. Nagasawa, *Science* **282**, 1874 (1998).
38. The supplementary data are available on *Science* Online at www.sciencemag.org/cgi/content/full/295/5557/1051/DC1.
39. This work was supported by NASA grants NAG5-10610 (A.N.K., P.I.), NAG5-4212 (K. Keil, P.I.), NAG5-4704 (K.D.M., P.I.), NAG5-10523 (L.A.L., PI), and NAG5-7396 and NAG5-10468 (G.J.M., P.I.). This is Hawaii Institute of Geophysics and Planetology publication 1145 and School of Ocean and Earth Science and Technology publication 5928.

The Mantle Flow Field Beneath Western North America

P. G. Silver[1]* and W. E. Holt[2]

Although motions at the surface of tectonic plates are well determined, the accompanying horizontal mantle flow is not. We have combined observations of surface deformation and upper mantle seismic anisotropy to estimate this flow field for western North America. We find that the mantle velocity is 5.5 ± 1.5 centimeters per year due east in a hot spot reference frame, nearly opposite to the direction of North American plate motion (west-southwest). The flow is only weakly coupled to the motion of the surface plate, producing a small drag force. This flow field is probably due to heterogeneity in mantle density associated with the former Farallon oceanic plate beneath North America.

It is surprising that after more than three decades into the plate tectonic revolution, we have so little direct observation of the mantle flow field that accompanies plate motion. The most straightforward measure of mantle flow is provided by the trajectory of subducted slabs whose seismicity and high seismic velocities provide tracers of the flow. Yet even in subduction zone environments there is evidence for complex three-dimensional flow both above and below the slab (*1–4*). Far from slabs, even less information is available to delineate the mantle flow field. Various approaches have been used to predict this flow field theoretically. One approach (*5, 6*) calculates the mantle flow field that would result if the motions of the plates are imposed as boundary conditions, in addition to considering the trenches and ridges as sources and sinks of mass. This flow field is dominated by plate-entrained flow and a corresponding counterflow. More recently, several groups have calculated the instantaneous field arising from density anomalies in the mantle

inferred from either seismic tomography or the history of subduction (*7, 8*). The plates are again taken as boundary conditions on this flow field, and a plate velocity is chosen such that the integrated torque on each plate vanishes. Both approaches adequately predict plate velocities, although the accompanying mantle flow fields and driving forces are different. The major difference in these approaches has to do with the role of density anomalies that are not directly attached to currently subducting plates, but are either inferred from global seismic tomography or from the long-term history of subduction. One way of testing these models is to measure the flow field beneath a plate that is not attached to a slab, but that has a mantle density anomaly beneath it and therefore different mantle flow fields predicted by (*5, 6*) and (*7, 8*). The North American plate has these characteristics (*9*).

Here we provide such a test, using a new procedure for inferring mantle flow velocity beneath western North America through the simultaneous analysis of surface deformation data [from Global Positioning System (GPS) and Quaternary fault slip data] and mantle deformation inferred from seismic anisotropy. Westernmost North America is ideal in particular because there is little lithosphere beneath the crust (*10–12*). This means that the anisotropy is dominated by the differential horizontal motion between the lithosphere and underlying

mantle, producing a deformation fabric in the asthenosphere (*13*), associated with simple shear (*14*). The magnitude and direction of horizontal shear within the asthenosphere depends on the vector difference, V_ϕ, between the horizontal velocity of the lithosphere, V_ℓ, and the horizontal component of velocity of the mantle, V_m, at the base of the asthenosphere (*15*). Writing $V_m(\hat{r}) = r_a\omega_m \times \hat{r}$, $V_p(\hat{r}) = r_e\omega_p \times \hat{r}$, and $V_\ell(\hat{r}) = V_p(\hat{r}) + V_t(\hat{r})$, this vector difference can be expressed as

$$V_\phi(\hat{r}) = r_e\omega_p \times \hat{r} + V_t(\hat{r}) - r_a\omega_m \times \hat{r}$$

(1)

where r_e is Earth's radius, ω_p is the angular velocity for the stable portion of the plate, $V_t(\hat{r})$ is the lithosphere velocity relative to the stable portion of the plate [i.e., $V_t(\hat{r}) = 0$ for a rigid plate], ω_m is the angular velocity of the mantle at the base of the asthenosphere at radius r_a, and $\hat{r}$ is Earth's position unit vector (*16*).

The orientation of $V_\phi(\hat{r})$ can be constrained from seismic anisotropy; for finite strains of order unity, the *a* axis of olivine tends to orient parallel to the flow line (*17*) and hence parallel to $V_\phi(\hat{r})$. For a vertically propagating shear wave recorded at a single station, the fast polarization direction, ϕ, of a split shear wave will be parallel to $V_\phi(\hat{r})$ as well (*14*). If we have an observation of ϕ, we can then express the orientation of $V_\phi(\hat{r})$ as $\hat{V}_\phi(\hat{r}) = \pm\hat{V}_s(\hat{r})$, where $\pm\hat{V}_s(\hat{r})$ denotes the orientation of ϕ subject to a 180° ambiguity. Within or across a plate boundary zone, where $V_t(\hat{r})$ changes as a function of $\hat{r}$, the three components of ω_m in Eq. 1 can be uniquely determined with as few as three observations of ϕ (Fig. 1) (*18*).

We used splitting data from only the red areas of Fig. 2, where asthenospheric flow is likely to dominate the anisotropic contribution (*19*). For $\hat{V}_s(\hat{r})$ in this western region, we used data from a recent study (*20*) augmented by additional data in the region (*14, 21*) (Fig. 2). For $V_t(\hat{r})$, we used the interpolated surface velocity field (*22, 23*) derived from GPS observations (*24–33*) and Quaternary fault slip rates (*34, 35*).

[1]Department of Terrestrial Magnetism, Carnegie Institution of Washington, Washington, DC 20015, USA. [2]State University of New York, Stony Brook, NY 11794, USA.

*To whom correspondence should be addressed. E-mail: silver@dtm.ciw.edu